Fully-Automated Adaptive Mesh Refinement for Media Embedding Complex Heterogeneities: Application to Poroelastic Fluid Pressure Diffusion

Marco Favino Jürg Hunziker
Eva Caspari
Beatriz Quintal Rolf Krause
Klaus Holliger

March 22, 2021

Abstract Relating the attenuation and velocity dispersion of seismic waves to fluid pressure diffusion (FDP) by means of numerical simulations is essential for constraining the mechanical and hydraulic properties of heterogeneous porous rocks. This, in turn, is of significant importance for a wide range of prominent applications throughout the Earth, environmental, and engineering sciences, such as, for example, geothermal energy production, hydrocarbon exploration, nuclear waste disposal, and CO_2 storage. In order to assess the effects of wave-induced FDP in heterogeneous porous rocks, we simulate time-harmonic oscillatory tests based on a finite element (FE) discretization of Biot's equations in the time-frequency domain for representative elementary volumes (REVs) of the considered rock masses. The major challenge for these types of simulations is the creation of adequate computational meshes, which resolve the numerous and complex interfaces between the heterogeneities and the embedding background. To this end, we have developed a novel method based on adaptive mesh refinement (AMR), which allows for the fully automatic creation of meshes for strongly heterogenous media. The key concept of the proposed method is to start from an initially uniform coarse mesh and then to gradually refine elements which have non-empty overlaps with the embedded heterogeneities. This results in a hierarchy of non-uniform meshes with a large number of elements close to the interfaces, which do, however, not need to be explicitly resolved. This dramatically simplifies and accelerates the laborious and time-consuming process of meshing strongly heterogeneous poroelastic media, thus enabling the efficient simulation of RVEs containing heterogeneities of quasi-arbitrary complexity. After a detailed description of the methodological foundations, we proceed to demonstrate that the FE discretization with low-order FE has a unique

solution and hence does not present spurious modes. We assess the practical effectiveness and accuracy of the proposed method by means of four case studies of increasing complexity.

keywords adaptive mesh refinement; finite element method; Biot's equations; poroelasticity; fluid pressure diffusion; seismic attenuation and velocity dispersion

1 Introduction

In the mesoscopic scale range, that is, at scales larger than the pore size but smaller than the seismic wavelength, the attenuation and velocity dispersion of seismic waves in heterogeneous porous rocks tends to be dominated by fluid pressure diffusion (FDP) [59, 44, 32, 47, 43]. The analysis of these characteristics thus has the potential of revealing valuable information on the prevailing mechanical and hydraulic properties of the probed subsurface regions. This, in turn, is relevant for many applications, such as geothermal energy production, hydrocarbon exploration, nuclear waste disposal, and CO_2 storage.

In order to quantify the effects of FPD in fluid-saturated heterogenous porous rocks, time-harmonic oscillatory tests are simulated employing Biot's equations of poroelasticity for representative elementary volumes (REVs) of the considered geological units [6, 7, 8]. This allows to evaluate the seismic response of such REVs in terms of their frequency-dependent seismic attenuation and velocity dispersion characteristics [53]. The primary motivation for this upscaling-type approach is that simulating wave propagation in poroelastic media is computationally inefficient [16, 37], as wave propagation and FPD prevail at significantly different time scales [17]. Time-harmonic oscillatory tests are generally performed at frequencies at which inertial effects can be ignored and hence are also referred to as quasi-static tests [39]. For most of fluid-saturated porous rocks, inertial effects do indeed become significant only at ultrasonic frequencies [11].

For the simulation of heterogeneous porous and/or fractured porous rocks of realistic complexity with a finite element (FE) method, meshing is arguably the major bottleneck. The creation of computational grids that resolve the numerous complex interfaces associated with the embedded heterogeneities remains an immensely tedious and error-prone task, which tends to require a high degree of human interaction. This finds its expression in the fact that, although a wide range of models and numerical methods have been proposed to improve the accuracy and efficiency of the simulation of FDP in heterogenous porous media [39, 53, 49], corresponding applications have so far been limited to simple geometries of the heterogeneities and/or to small numbers of complex features [40, 52, 48].

Adaptive mesh refinement (AMR) is a highly-effective method for improving the accuracy of numerical simulations of differential problems while retaining their computational efficiency. These techniques can reduce by orders-of-magnitude the number of degrees of freedom necessary to reach a prescribed

accuracy. AMR may be employed together with *error estimators* following the paradigm "Solve-Estimate-Refine" [20, 34, 57, 18, 19, 50] or, alternatively, it can be used exploiting *a-priori* information on the problem. For example, AMR has been used to create meshes for hybrid-dimensional fracture-matrix models, i.e., models where a two-dimensional background medium is coupled with one-dimensional embedded fractures. In [38], AMR is used to generated meshes in a domain with discrete fracture networks together with constrained Delaunay triangulations, thus resulting in a conforming mesh that is denser at fracture locations. In [46], an initially uniform mesh of the background medium is adaptively refined in the vicinity of the lower-dimensional fractures. This approach results in a non-conforming mesh, which allows for a more adequate representation of flow and transport phenomena between the background and the fractures. Another application of a non-conforming method can be found in [4] for the simulation of wave propagation in heterogeneous media. Here, mesh adaptation was driven by the local wave velocity and the maximum frequency of interest.

In previous works [29, 30], we presented initial applications of a novel method based on AMR, which enables fully automated meshing of complex heterogeneous structures, such as stochastic fracture networks. Inspired by the adaptive schemes proposed in [4, 15, 46], our method does not create meshes which explicitly resolve the heterogeneities. Instead, it creates sequences of non-conforming quadrilateral or hexahedral structured meshes, which approximate the heterogeneities with increasing accuracy. To this end, the embedded heterogeneities are analytically defined as subsets of the computational domain under consideration. Hence, starting from a uniform coarse mesh, elements which have non-empty overlaps with the interfaces between background and the embedded heterogeneities are successively refined. This allows to automatically create a hierarchy of non-conforming nested meshes, which are finer near the interfaces where numerical errors tend to be concentrated. As in [4], meshes are enforced to be 1-irregular and the discretization is performed with a conforming FE method. We explicitly construct the stiffness matrix since we use an implicit method.

The proposed method can indeed be regarded as a generalization of the Finite Cell Method (FCM) [22]. The core idea of the FCM is to immerse a smaller complicated physical domain into a larger and simpler one and then to use locally refined, axis-aligned meshes for the embedding domain to describe the features of the immersed domain. Hence, the differential problem is solved by extending the material properties to zero in the embedding domain. In our study, we can consider the REV as the embedding domain and the heterogeneities as the immersed domain.

While our method has already allowed us to perform simulations of oscillatory tests for media containing complex fracture networks of unprecedented realism and complexity [29, 30], it has never been formally introduced and its numerical properties were, as of yet, largely unexplored. The main objective of this work is thus to provide a formalization of the proposed AMR method. In doing so, we also seek to demonstrate that the employed discretization of Biot's

equations with low-order FEs has a unique solution and, hence, does not present any instabilities, such as spurious modes [13, 24, 25]. Moreover, we explore the method's convergence by means of numerical examples.

The manuscript is organized as follows. In section 2, we describe our mathematical model based on Biot's consolidation equations in the frequency domain and the time-harmonic oscillatory tests used to compute the seismic attenuation and velocity dispersion characteristics. In section 3, we outline the FE formulation. Section 4 presents our AMR methodology, which is then validated in section 5 by means of four numerical tests. Two tests, for which analytical solutions are available, are used to explore the convergence properties of our method. In the third test, we compare the results obtained with our adaptive method against those obtained on a mesh which explicitly resolves the interfaces separating different materials. Finally, we illustrate the convergence of our method for the particularly challenging scenario of a realistic stochastic fracture network. In the appendices, we formally derive the weak formulation of the problem with a particular focus on the use of complex variables and we prove the stability of its FE formulation.

2 Mathematical model

To find the effective seismic attenuation and velocity dispersion of a heterogeneous porous and/or fractured rock mass, a corresponding REV is modeled as a poroelastic medium with non-constant heterogeneous coefficients [31]. That is, different material properties are assigned to the background and to the embedded heterogeneities. In the following, we present the mathematical model, which we employ to simulate the oscillatory tests performed over an REV. It consists of Biot's consolidation equations in the frequency domain with periodic boundary conditions. The weak formulation of this model is formally derived in Appendix A.

2.1 Computational domain

We denote by the integer $d \in \{2, 3\}$ the spatial dimension of the problem and we assume that the domain on which the equations are defined is $\Omega = (-\mathrm{L}, \mathrm{L})^d$ with $\mathrm{L} \in \mathbb{R}$ representing the half-length of the side of the REV. Over Ω, we introduce a set $\mathcal{F}$ of d-dimesional heterogeneities $f_i \subset \Omega$ with $i = 1, 2 \ldots N_f$, where $N_f = |\mathcal{F}|$ is the number of heterogeneous inclusions. The subdomain Ω_f denotes the set of all inclusions, i.e., $\Omega_f = \bigcup_{i=1}^{N_f} f_i$. We also set $\Omega_b = \Omega \backslash \Omega_f$. In this way, Ω admits the decomposition $\Omega = \Omega_b \cup \Omega_f$ with $\mathring{\Omega}_b \cap \mathring{\Omega}_f = \emptyset$. We denote by $\underline{n}$ the outward normal and by $\mathbf{x}$ the points of Ω such that x_i is the i-th Cartesian coordinate with $i = 1, \ldots, d$.

We also introduce the symbol Γ_α^i to denote the $(d-1)$-dimensional subset of Ω defined as

$$\Gamma_\beta^i = \{\mathbf{x} \in \overline{\Omega} \,:\, x_i = \beta\}.$$

In this way, the boundary of Ω admits the decomposition

$$\partial\Omega = \sum_{\mathrm{s}\in\{-1,1\}} \sum_{i=1}^{d} \Gamma^i_{\mathrm{sL}}.$$

2.2 Biot's consolidation equations

To simulate FPD in an REV, we employ Biot's consolidation equations of poroelasticity [5, 58] in the so-called $\underline{u}$-p form. Since we are interested in the simulation of time-harmonic oscillatory tests, we write them in the frequency domain [49], where the unknowns are the solid displacement $\underline{u}(\,\cdot\,;\omega)$ and the fluid pressure $p(\,\cdot\,;\omega)$, which are both complex functions. The parameter ω denotes the angular frequency. Neglecting inertial terms, Biot's equations in the frequency domain are

$$-\mathrm{div}\ \underline{\underline{\sigma}} = 0, \quad \text{in } \Omega, \tag{1}$$

$$-\,\mathrm{j}\,\alpha\,\mathrm{div}\,\underline{u} - \mathrm{j}\,\frac{p}{M} + \frac{1}{\omega}\mathrm{div}\left(\frac{k}{\eta}\nabla p\right) = 0, \quad \text{in } \Omega, \tag{2}$$

where j is the imaginary unit, k the permeability, η the dynamic shear viscosity of the fluid, and α the so-called Biot or Biot-Willis coefficient. Please note that the dependence of $\underline{u}$ and p on ω has been dropped for ease of notation.

The total stress tensor $\boldsymbol{\sigma}$ is a function of the strain

$$\underline{\underline{\varepsilon}}(\underline{u}) := \frac{\nabla\underline{u} + \nabla\underline{u}^T}{2} \tag{3}$$

and of the pressure p and can be written as

$$\underline{\underline{\sigma}} = 2\mu\underline{\underline{\varepsilon}}(\underline{u}) + \lambda\mathrm{tr}\underline{\underline{\varepsilon}}(\underline{u})\,\underline{\underline{I}} - \alpha p\underline{\underline{I}}, \tag{4}$$

where μ is the shear modulus of the dry frame and λ the Lamé parameter. Because of (3), the stress tensor is symmetric but not Hermitian ($\sigma_{ij} = \sigma_{ji}$ and $\sigma_{ij} \neq \sigma^*_{ji}$). It remains to define α and M, which are given by

$$\alpha = 1 - \frac{K_b}{K_s} \text{ and } \frac{1}{M} = \frac{\phi}{K_f} + \frac{\alpha - \phi}{K_s}, \tag{5}$$

with ϕ denoting the porosity and K_f, K_s, and K_b the bulk moduli of the fluid, the solid grains, and the dry frame, respectively.

Equations (1) and (2) are subjected to the following periodic boundary conditions

$$\underline{u}|_{\Gamma^i_{\mathrm{L}}} - \underline{u}|_{\Gamma^i_{-\mathrm{L}}} = \underline{\alpha}_i \quad \text{with } i = 1,\ldots,d, \tag{6}$$

$$\underline{\sigma}_i|_{\Gamma^i_{\mathrm{L}}} - \underline{\sigma}_i|_{\Gamma^i_{-\mathrm{L}}} = \underline{0} \quad \text{with } i = 1,\ldots,d, \tag{7}$$

$$p|_{\Gamma^i_{\mathrm{L}}} - p|_{\Gamma^i_{-\mathrm{L}}} = 0 \quad \text{with } i = 1,\ldots,d, \tag{8}$$

$$\frac{k}{\eta}\frac{\partial p}{\partial x_i}|_{\Gamma^i_{\mathrm{L}}} - \frac{k}{\eta}\frac{\partial p}{\partial x_i}|_{\Gamma^i_{-\mathrm{L}}} = 0 \quad \text{with } i = 1,\ldots,d. \tag{9}$$

Equation (6) imposes the continuity of the displacements up to an external relative displacement $\underline{\alpha}_i$. In equation (7), $\underline{\sigma}_i$ denotes the i-th column of the stress tensor. This equation is derived from the continuity of the stress at two extrema of the domain

$$(\underline{\underline{\sigma}}\,\underline{n})|_{\Gamma^i_{\mathrm{L}}} = -(\underline{\underline{\sigma}}\,\underline{n})|_{\Gamma^i_{-\mathrm{L}}}.$$

Considering, for example, the first direction with $d = 2$, we observe that the normals are $(-1, 0)$ at $x_1 = -\mathrm{L}$ and $(1, 0)$ at $x_1 = \mathrm{L}$. Hence, we obtain

$$-\underline{\sigma}_1|_{\Gamma^1_{\mathrm{L}}} = -\underline{\sigma}_1|_{\Gamma^1_{-\mathrm{L}}}.$$

The material properties μ, λ, α, M, and k/η in Biot's equations are assumed to be real functions attaining constant positive values over Ω_b and Ω_f, such as, for example,

$$\mu = \begin{cases} \mu_b, & \text{in } \Omega_b, \\ \mu_f, & \text{in } \Omega_f. \end{cases} \tag{10}$$

2.3 Time-harmonic oscillatory tests

Time-harmonic oscillatory tests are realized by imposing a relative displacement along one direction between two opposite faces of the boundary of the domain and setting to zero the relative displacement along the other directions. For isotropic samples, these tests can be performed in any of the d axes of the considered problem. We carry out two different tests:

1. a compression test to determine P-wave attenuation and velocity dispersion;
2. a shear test to obtain the corresponding S-wave characteristics of the medium.

Considering, for example, tests in $d = 2$ along the second (vertical) direction, the former is realized by setting $\underline{\alpha}_2 = [0;\, \alpha]$ and the latter by setting $\underline{\alpha}_2 = [\alpha;\, 0]$, with $\alpha \in \mathbb{R}$, while setting $\underline{\alpha}_1 = \underline{0}$.

By averaging specific components of the calculated stress and strain tensors, we obtain the complex P-wave modulus $H(\omega)$ and the complex S-wave modulus $\mu(\omega)$ for the second direction as [41]

$$H(\omega) = \frac{\bar{\sigma}_{22}(\omega)}{\bar{\varepsilon}_{22}(\omega)} \quad \text{and} \quad \mu(\omega) = \frac{\bar{\sigma}_{12}(\omega)}{2\bar{\varepsilon}_{12}(\omega)}, \tag{11}$$

where the bars denote spatially averaged quantities. The factor 2 in the denominator of the shear modulus is due to the Voigt notation [41]. To calculate the inverse quality factor $1/Q(\omega)$ quantifying the attenuation, one simply divides the imaginary part of these moduli by the corresponding real part [41]

$$\frac{1}{Q_p(\omega)} = \frac{\Im\{H(\omega)\}}{\Re\{H(\omega)\}} \quad \text{and} \quad \frac{1}{Q_s(\omega)} = \frac{\Im\{\mu(\omega)\}}{\Re\{\mu(\omega)\}}. \tag{12}$$

The frequency-dependent velocity $V(\omega)$ is then obtained by

$$V_p(\omega) = \sqrt{\frac{\Re\{H(\omega)\}}{\bar{\rho}}} \text{ and } V_s(\omega) = \sqrt{\frac{\Re\{\mu(\omega)\}}{\bar{\rho}}}, \tag{13}$$

where $\bar{\rho}$ denotes the average bulk density of the sample.

If the sample is anisotropic, a horizontal compression test is needed in addition to the vertical compression and the shear tests. This is realized by setting $\underline{\alpha}_1 = [\alpha; 0]$ and $\underline{\alpha}_2 = \underline{0}$. Following the procedure described by [51], these three tests allow for inferring the frequency-dependent equivalent Voigt stiffness matrix $\underline{\underline{C}}$. For the general anisotropic case with $d = 2$ under plane strain conditions, $\underline{\underline{C}}$ relates the mean strain to the mean stress

$$\begin{pmatrix} \bar{\sigma}_{11} \\ \bar{\sigma}_{22} \\ \bar{\sigma}_{12} \end{pmatrix} = \begin{pmatrix} C_{11} & C_{12} & C_{16} \\ C_{12} & C_{22} & C_{26} \\ C_{16} & C_{26} & C_{66} \end{pmatrix} \begin{pmatrix} \bar{\varepsilon}_{11} \\ \bar{\varepsilon}_{22} \\ 2\bar{\varepsilon}_{12} \end{pmatrix}. \tag{14}$$

Once the complex components of $\underline{\underline{C}}$ have been determined, one can solve for the wavenumbers of the P- and S-waves, which can then be related to the frequency- and angle-dependent attenuation and velocity characteristics $1/Q(\omega, \theta)$ and $V(\omega, \theta)$ [51], where θ denotes the incidence angle with regard to the vertical axis.

3 Finite element method on adapted non-conforming meshes

Before discussing the FE approximation on non-conforming meshes, we first introduce some definitions (adapted from [18]) which will simplify the presentation.

1. **Mesh $\mathcal{T}$.** A mesh $\mathcal{T}$ is a triangulation of Ω into squared ($d = 2$) or cubic ($d = 3$) elements. Elements will be denoted by K and h_K denotes the side length of K.

2. **Red-refinement.** We say that an element K of side length h_K is red-refined if it is split into 2^d identical elements of side length $h_K/2$.

3. **Initial mesh $\mathcal{T}_0$.** The mesh $\mathcal{T}_0$ is supposed to be a uniform, regular triangulation of Ω into closed elements.

4. **Adapted mesh $\mathcal{T}_{\mathscr{L}}$.** A mesh $\mathcal{T}_{\mathscr{L}}$, with $\mathscr{L} > 1$ is obtained by a finite number $\mathscr{L}$ of red-refinements from $\mathcal{T}_0$, where for every $\ell = 1, ..., \mathscr{L}$, $\mathcal{T}_\ell$ is obtained by a red-refinement of a subset $\mathcal{A}$ of elements of $\mathcal{T}_{\ell-1}$. Then, one says that $\mathcal{T}_\ell$ is some red-refinement of $\mathcal{T}_{\ell-i}$, with $i = 1, \ldots, \ell$. The symbol $E(K)$ denotes the number of refinements that has been applied to its parent element in $\mathcal{T}_0$ in order to obtain K.

5. **Hanging nodes.** Given a mesh $\mathcal{T}$, which is some red-refinement of $\mathcal{T}_0$, a node is said to be *hanging* if it belongs to an element K but it is not a vertex of such an element. Otherwise, the node is called *regular*. We will refer to hanging nodes belonging to an edge as *edge hanging nodes* and to hanging nodes belonging to a face as *face hanging nodes*.

6. **k-irregular meshes.** If any edge contains at most k hanging nodes in its inside, $\mathcal{T}$ is called k-irregular. We denote the number of all hanging nodes by N^h and the number of all regular nodes by N^r.

According to the definitions above, a triangulation can be non-conforming and non-uniform but all elements are shape-regular, being squares or cubes. In particular, 1-irregular meshes, also referred to as balanced meshes [4], have the constraint that each element has at most 2^{d-1} identical adjacent elements per side. Examples of 1-irregular meshes for $d = 2$ are shown in Figure 1.

Both finite difference [3] and FE [61] approximations have been proposed on adapted meshes. The main advantages of employing adapted meshes composed of quadrilateral and hexahedral elements stems from their capacity of resolving heterogeneities and complex features in the domain, while keeping a regular shape of the elements. This, in particular, allows to reduce ill-conditioning due to too skewed elements at the price of having non-constant and non-regular material properties over some elements. Hence, interfaces are not explicitly represented but approximated with an order of $\mathcal{O}(h)$.

Both the displacement $\underline{u}$ and the pressure p are locally approximated on each element with bilinear or trilinear functions. Such functions provide greater accuracy compared to linear functions on triangles and tetrahedra: the asymptotic convergence rate is the same but the constant in the convergence estimate is typically smaller. The computation of the local stiffness matrices is performed by standard numerical quadrature, assigning different material properties to each quadrature point. At the global level, only degrees of freedom associated with regular nodes are considered, meaning that the size of the linear system arising from the FE discretization is $(d + 1)N^r$, i.e. N^r-times the number of variables involved in the model. The values at the hanging nodes are subsequently computed by interpolation: components of the solution at an edge hanging node are imposed to be the average of the solution at its two edge neighbors and components at a face hanging node are imposed to be the average of the solution at its four face neighbors.

Although the equations (1)-(4) define a generalized saddle-point problem, its approximation with a low-order FE method provides a unique solution and does not present instabilities, such as spurious modes. In Appendix B, we formally prove the uniqueness of the solution. Here, we want to briefly state that the presence of a diffusion term in equation (2) drastically changes the *inf-sup* condition for this system of equations [13, 24, 25], allowing also for approximations of the same order for $\underline{u}$ and p.

The definitions outlined at the beginning of this section refer to the specific case of square or cubic domain and for discretizations based on axis-aligned

quadrilateral and hexahedral elements. They can be generalized to any domain with polygonal boundaries and to any kind of triangulation, in particular triangles and non-axis-aligned quadrilaterals for two-dimensional cases [18], as well as, tetrahedra and non-axis-aligned hexahedra for three-dimensional cases. For the case of general quadrilaterals and hexahedra, standard convergence proofs have to be adapted due to the presence of a non-affine map from the reference element to a generic element [10].

4 Adaptive mesh refinement

4.1 Adaptive mesh refinement for heterogenous media

The main goal of our work is to perform simulations of FPD employing equi-dimensional models, i.e. models where d-dimensional fractures are embedded into a d-dimensional matrix. For realistic cases involving multiple complex fracture networks, this process is prohibitively time-consuming and requires an excessive degree of human-interaction. To alleviate this problem, we propose a method based on AMR to automatically mesh complex embedded fractures.

The basic idea of the method is to start with a coarse initial mesh and, given a distribution of embedded heterogeneities, refine the elements that have non-empty intersections with them. By iterating this procedure, we can create a hierarchy of meshes, which become progressively finer towards the discontinuities and which feature element boundaries that do not coincide with them. This AMR method allows to automatically create meshes for any heterogeneity distribution without any human interaction. In order to evaluate the accuracy of the method, solutions or output variables, such as seismic attenuation and velocity dispersion, from two consecutive hierarchical levels can be compared.

Another possibility for evaluating the quality of the solution would be to employ error estimators, which are not readily available for the proposed method. In this regard, there are basically two options. One would be to adapt error estimators based on flux reconstruction that have already been developed for Biot's equations in the time domain [50]. Here, the main difficulty would be to extend this methodology to complex vector spaces and non-symmetric problems. Another would be to use more generic residual-based error estimators for coupled problems, e.g. [23].

4.2 Algorithm and implementation

Figure 2 represents the algorithmic details of the proposed AMR method for level $\ell = 1, \dots \mathcal{L}$. We assume that mesh $\mathcal{T}_0$ is regular, uniform, and structured, hence, the number of elements is $N_0 = (2\mathrm{L}/h)^d$. At each level ℓ, we select a subset of *parent* elements $\mathcal{A}_{\ell-1} \subset \mathcal{T}_{\ell-1}$ and we red-refine all element $K \in \mathcal{A}_{\ell-1}$. The total number of elements in the mesh $\mathcal{T}_\ell$ is $N_\ell = N_{\ell-1} + (2^d - 1)|\mathcal{A}_{\ell-1}|$.

In Step 1 of the algorithm, all elements that have non-empty intersections with the boundary ∂f_i of at least one heterogenous inclusions are selected. Step

2 of the algorithm ensures that each mesh $\mathcal{T}_\ell$ is 1-irregular. It is important to notice that the outer loop in Step 2 has to be iterated until the set $\mathcal{A}_{\ell-1}$ is unchanged, because the elements added after the first loop may still have neighbouring elements that are too coarse to ensure that the mesh is at most 1-irregular.

Iterating Steps 1-3, the initial mesh $\mathcal{T}_0$ can be adapted for any given set of heterogeneous inclusions with an arbitrary accuracy depending on some *a-priori* criterion. In this way, we define a hierarchy of 1-irregular meshes that are finer close to the interfaces between the heterogeneities and the embedding background.

AMR is nowadays available in some of the most widely used free FE packages: Libmesh, which works both with triangular/tetrahedral meshes and quadrilateral/hexahedral meshes [33], MOOSE, which wraps and extends Libmesh functionalities [26], and Deal II, which works with quadrilateral and hexahedral meshes [2]. Software libraries based on octree data structures, such as, for example `p4est` [15], allow to easily generate and manage adapted hexahedral meshes, in which elements are recursively refined.

For a parallel implementation, assuming that the distribution of the mesh is balanced amongst the processors, the algorithm for marking elements for refinement scales ideally since it requires no communication between the processors. On the other hand, ensuring that the resulting mesh is 1-irregular requires communication between the processors to which different adjacent subdomains are assigned. In order to achieve this, the mesh requires the presence of a layer of ghost elements around each subdomain, which is usually available in FE meshes. The performance of the algorithm is thus primarily constrained by the actual refinement process, which depends on the implementation of the employed library.

5 Numerical results

In the following, we consider four numerical tests to demonstrate the effectiveness and the accuracy of the proposed AMR method in reproducing frequency-dependent seismic attenuation and velocity dispersion characteristics for a broad range of heterogeneous media. The first two tests, for which analytical solutions are available, serve to assess the convergence of the numerically estimated seismic attenuation and velocity dispersion characteristics to the corresponding analytical solutions. In the third test, we compare the results of our AMR method with those obtained on a mesh, which explicitly resolves the heterogeneities. In the fourth test, we explore the convergence properties of the proposed method for scenarios of very high complexity by applying it to a realistic stochastic fracture network.

For all two-dimensional tests presented in Subsections 5.1, 5.3, and 5.4, we consider an REV of a fractured medium consisting of a square with an edge length of $2\mathrm{L} = 400$ mm. The elements of the initial uniform mesh $\mathcal{T}_0$ have a side length of 4 mm. The material properties of the heterogeneities and of the

embedding background are listed in Table 1 and are representative of a tight sandstone [42]. Simulations have been performed up to a frequency of 10^6 Hz. Since the main interest of our work are FDP effects, the inertial term in our model has been neglected, and, hence, we neither consider wave propagation effects, such as diffraction and scattering, nor so-called Biot global flow. For the considered material properties, Biot global flow may start to come into the play at frequencies around 10^5 Hz. Correspondingly, this mechanism is not expected to affect our results significantly as reported in [30]. However, scattering might play a role for the model with fracture networks and thus would be an additional source of attenuation, which we do not take into account. In this context, it is, however, important to note that the proposed AMR method can be coupled with any different model.

All numerical tests have been implemented in the FE framework MOOSE. Inside MOOSE, we have developed the application named "Parrot", for the simulation of heterogeneous poroelastic materials based on Biot's equations in the time and time-frequency domain. The solution of the linear system arising from the FE discretization is performed by means of the parallel direct solver MUMPS [1].

The use of more advanced solution methods, such as multigrid or domain decomposition techniques, is far from trivial for the considered application. On the one hand, multilevel methods have been developed for saddle-point problems and on adaptively refined meshes [14, 54]. On the other hand, they have to be adapted to the specific multiscale problem [27]. In particular, due to the small size of the inclusions and the pronounced discontinuities associated with the material properties, the assembly of coarse grid operators has to be combined with the use of multiscale discretization methods. Potential pathways in this direction would be the use of composite FE [56], generalized FE [55], or multiscale FE [28].

5.1 Example 1: Horizontally layered medium

Here, we compare the attenuation and velocity dispersion characteristics obtained by our AMR method for a sample of a periodically layered medium with the corresponding analytical solution [60, 35]. As one of the key motivations for the development of the proposed AMR method was to allow for the accurate and efficient simulation of fractured media [29, 30], we represent one of the two alternating layers as a horizontal fracture with a thickness of 4 mm separated by a background layer with a thickness 196 mm, (Figure 3).

The elements of the initial uniform mesh $\mathcal{T}_0$ have a side length of 4 mm. As fractures are aligned with the horizontal coordinate axis and their thickness coincides with the initial mesh-size, we consider two different scenarios: 1) fractures coincide with a layer of mesh elements and hence they are exactly resolved by the mesh $\mathcal{T}_0$ and 2) fractures are shifted of 1/32 mm with respect to the initial mesh such that they are only resolved after 7 AMR steps.

In Table 2, we report the root mean square errors err_{Q_α}, with $\alpha \in \{p, s\}$, of the attenuation characteristics for an incident angle of 30° for the first 4 AMR

Table 1: Material properties used in example 1 with layer 1 being the background medium and layer 2 representing a fracture.

Property	Symbol	Unit	Layer 1 Background	Layer 2 Fracture
Thickness		m	0.196	0.004
Density of solid	ρ_s	kg/m^3	2700	2700
Density of the fluid	ρ_f	kg/m^3	1000	1000
Shear modulus of dry frame	μ	GPa	32	0.02
Permeability	k	m^2	10^{-18}	10^{-11}
Dynamic shear viscosity of the fluid	η	Pa·s	0.001	0.001
Porosity	ϕ	-	0.06	0.5
Bulk modulus of fluid	K_f	GPa	2.4	2.4
Bulk modulus of solid grains	K_s	GPa	40	40
Bulk modulus of dry frame	K_b	GPa	34	0.025

Table 2: Root mean square error of seismic attenuation for meshes which explicitly resolve the interface of a one-dimensional layered model (Table 1).

AMR level	err_{Q_p}	err_{Q_s}
0	0.08177	0.02219
1	0.00083	0.00011
2	0.00071	0.00011
3	0.00035	0.00010
4	0.00021	0.00010

levels for the scenario 1) and similar results have also been obtained for the scenario 2) in which fractures are not resolved by the mesh. The fact that we observe quasi-complete convergence after the first refinement step (Figure 4) shows that, for fractures aligned to one of the coordinate axes, there is no need to employ meshes that actually resolve fractures.

5.2 Example 2: Spherical inclusion

To assess the functionality of the proposed AMR method in a three-dimensional setting, we consider a classical patchy saturation problem, for which an analytical solution is available [47]. The underlying model corresponds to a porous sphere saturated with gas embedding another porous sphere saturated with water. Given that seismic attenuation prevails in the water-saturated sphere, effects related to the geometry of the embedding gas-saturated volume are expected to be negligible [36]. For this reason, the geometry of the embedding volume can be replaced with a cube for the computation of the numerical solution. The side length of the corresponding gas-saturated cube is 2L = 80 cm. The enclosed fluid-saturated sphere has a radius $R = 32$ cm and its center coincides with the center of the cube. The material properties are given in Table

3.

Table 3: Material properties of example 2 consisting of a gas-saturated cube (background) enclosing a water-saturated sphere (inclusion).

Property	Symbol	Unit	Spherical Inclusion	Background
Density of solid	ρ_s	kg/m^3	2700	2700
Density of the fluid / gas	ρ_f	kg/m^3	1010	160
Shear modulus of dry frame	μ	GPa	3	3
Permeability	k	m^2	10^{-12}	10^{-12}
Dynamic shear viscosity of the fluid	η	Pa·s	0.003	$2 \cdot 10^{-5}$
Porosity	ϕ	-	0.25	0.25
Bulk modulus of fluid	K_f	GPa	2.4	0.04
Bulk modulus of solid grains	K_s	GPa	40	40
Bulk modulus of dry frame	K_b	GPa	4	4

The initial uniform mesh consists of cube-shaped elements with a side length 5cm. Subsequently, the elements along the boundary of the embedded sphere are adaptively refined. The number of elements and nodes for each level are reported in Table 4. Figure 5 shows the initial coarse and uniform mesh and the first three adapted meshes. Since the boundaries of the elements do not coincide with the interfaces between different materials, an element can lie partially inside and outside the corresponding heterogeneity. The material properties are then non-uniform within an element and different values of the material properties are assigned while evaluating them at the quadrature points during the assembly of stiffness matrix.

Figure 6 compares the resulting P-wave attenuation and velocity dispersion characteristics with the analytical solution [47]. The discrepancies between the numerical and the analytical solutions, which are clearly visible for the initial mesh, diminish with increasing refinement levels and become sufficiently small at the fourth refinement. The remarkably rapid convergence of the numerical

Refinements	Elements	Total nodes	Regular nodes	Hanging nodes
0	4096	4913	4913	0 (0.0%)
1	9528	12619	6567	6052 (48.0%)
2	33944	46299	16215	30084 (65.0%)
3	134464	184205	57831	126374 (68.6%)
4	535200	733279	223509	509770 (69.5%)
5	2135400	2926093	883091	2043002 (69.8%)
6	8543536	11705489	3523723	8181766 (69.9%)

Table 4: Mesh characteristics of each level of the proposed AMR method for the spherical inclusion shown in Figure 5. The number of hanging nodes is large since the refinement is performed only at the surface of the sphere.

Refinements	Elements	Total nodes	Regular nodes	Hanging nodes
0	10000	10201	10201	0 (0.0%)
1	10606	10925	10689	236 (2.2%)
2	11860	12423	11699	724 (5.8%)
3	14332	15377	13689	1688 (11.0%)
4	19300	21315	17687	3628 (17.0%)
5	35782	39729	32237	7492 (18.9%)
6	87958	95765	80553	15212 (15.9%)
7	272776	288309	257645	30664 (10.6%)

Table 5: Mesh characteristics of each level of the AMR method for the example involving two intersecting fractures. The fraction of hanging nodes increases up to the 5th refinement and then starts to decrease.

solution to the analytical one demonstrates the viability of our AMR method for three-dimensional scenarios.

5.3 Example 3: Two intersecting fractures

In this test, we compare the results obtained by our AMR method against those obtained on a mesh which explicitly resolves the interfaces between two intersecting fractures and their embedding background (Figure 7a). One fracture is vertical while the other is inclined by 45°. Both fractures have a length and a thickness of 200 mm and 0.5 mm, respectively

The triangular mesh which explicitly resolves the interfaces has been generated using the commercial software package COMSOL Multiphysics (Figure 7b). The AMR-based hierarchy of meshes has been computed with the subsequent application of six refinement steps to the initial mesh $\mathcal{T}_0$ (see Figures 7d through 7k for the finest four levels). The number of elements and nodes for each level are reported in Table 4. The resulting final mesh has a minimum side length of 0.0625 mm inside the fractures, and, hence, the fracture aperture is 8 elements wide. We observe how all elements overlapping with the fracture, which is modeled as a rectangle with 90° corners, are gradually refined to improve the resolution of the fracture tip. This illustrates the effectiveness of the meshing algorithm.

The P- and S-wave attenuation and velocity dispersion characteristics are computed for vertical incidence (0° angle) employing the material properties reported in Table 1. We consider the attenuation and velocity dispersion inferred from the time-harmonic oscillatory tests using the triangular mesh to be the reference solution of the problem, because (1) the triangular mesh explicitly follows the geometry of the fractures and (2) the triangular mesh is significantly denser in the vicinity of the fractures than the quadrilateral mesh. The corresponding results are shown in Figure 8. The bold gray line represents the reference solution, while the colored dashed lines depict the results of AMR levels 3 through 6 for our method. The intermediate results obtained after three

levels (blue dashed line) show no attenuation and velocity dispersion as the mesh is still too coarse to capture the fractures. This finds its expression in correspondingly small values of the real component of the fluid pore pressure distribution in Figure 9. In the fourth adaptive level (red dash-dotted line), the algorithm starts to resolve the fractures, but the calculated attenuation and velocity dispersion, as well as the underlying pore fluid pressure, still differ from those obtained for the triangular mesh. The fifth step (yellow dotted line) then provides results close to the reference solution and allows to reproduce the two attenuation peaks present. The sixth step (purple solid line) produces only minor additional improvements. Correspondingly, the distribution of the pore fluid pressure (Figure 9b, Figure 9c, and Figure 9d) gradually approaches that of the reference solution (Figure 9e). This case study demonstrates that an automatically refined mesh is able to accurately estimate the attenuation and velocity dispersion characteristics of a two-dimensional fractured medium.

5.4 Example 4: Stochastic fracture networks

The key motivation for the development of the proposed AMR method was to enable the fully automatic generation of meshes for models containing large numbers of highly complex heterogeneities. In this example, we therefore consider a realistic stochastic fracture network (Figure 10), which, at present, arguably represents one of the most complex and most challenging scenarios to mesh and simulate.

Fractures length is drawn from a scale-invariant power law distribution [21]. The fractures orientation is uniformly distributed between 30° and 150°, where 0° is a vertical fracture and 90° a horizontal one. The thickness of the fractures is constant at 0.5 mm. The positions of the center points of the fractures are drawn from a uniform distribution. As illustrated in Figure 10, fractures that cross the boundary of the sample are reintroduced on the other side of the sample, thus, making the model periodic in accordance with the corresponding periodic boundary conditions. Six AMR steps have been applied to the initial mesh $\mathcal{T}_0$ at the fracture locations. The resulting number of elements and nodes for each level are reported in Table 4.

The P- and S-wave attenuation curves, calculated for incident angles of 0°, 45°, and 90° are shown in Figure 11. As in the previous example, we observe that the intermediate results obtained after three AMR steps do not show any attenuation as the mesh is still too coarse to capture fractures. In the fourth level, fractures start to be resolved but the obtained values of the P- and S-wave attenuation still differs from those of the subsequent refinement levels. Finally, we observe that the differences between the fifth and sixth refinement steps are negligible, thus indicating convergence of the AMR method.

Refinements	Elements	Total nodes	Regular nodes	Hanging nodes
0	10000	10201	10201	0 (0.0%)
1	19729	22219	17753	4466 (20.1%)
2	46537	54080	39689	14391 (26.6%)
3	111220	130129	93240	36889 (28.3%)
4	272608	315245	231193	84052 (26.7%)
5	714802	806381	624844	181537 (22.5%)
6	2062852	2253776	1874112	379664 (16.8%)
7	6599809	6990669	6212029	778640 (11.1%)

Table 6: Mesh characteristics of each level of the AMR method for the stochastic fracture network example (Figure 10). The fraction of hanging nodes increases up to the 4th refinement and then starts to decrease.

6 Conclusions

We have presented a novel AMR method for the simulation of FPD in heterogeneous poroelastic media based on Biot's consolidation equations in the time-frequency domain. The proposed method uses non-conforming meshes and local hierarchical refinements, which allow to automatically and efficiently adapt an initially uniform mesh for any kind of heterogeneities. The idea is to start from a coarse and uniform mesh of an REV of a heterogeneous porous medium. Then, by refining the elements that have non-empty overlaps with the heterogeneities, we gradually adapt this initial mesh to resolve the embedded heterogeneities with increasing accuracy. This automatically creates a hierarchy of meshes for any kind of heterogeneities without any human interaction. On the thus adapted meshes, a discretization based on low order FE of Biot's consolidation equations is employed to simulate time-harmonic oscillatory tests, which allows to quantify the effects of FPD in terms of the seismic attenuation and velocity dispersion. For the proposed discretization, we have shown the uniqueness of the solution, thus ensuring that it does not present spurious modes.

Three numerical examples illustrate the accuracy of the method. In particular, we show that refining the mesh near the interfaces of the heterogeneities is sufficient and, that, there is no need for creating meshes that explicitly resolve such interfaces. We also demonstrated that for complex stochastic fracture networks, our AMR method exhibits rapid convergence of the seismic attenuation and velocity dispersion characteristics. This underlines the computational efficiency of the proposed method and its capacity of fully automatically meshing extremely complex heterogeneous media.

Our AMR method is based on the *a-priori* information that, for heterogeneous materials, numerical errors are localized at the interfaces. This was indeed corroborated by our numerical tests. Obviously, the development of an error estimator for Biot's equations in the frequency domain would also provide a criterion to control such numerical errors.

In the future, the resulting hierarchy of meshes could also be considered in the context of a multilevel solution strategy to replace the parallel direct solver we employed in the presented simulations.

Acknowledgements Marco Favino acknowledges gratefully the support of the Swiss National Science Foundation (SNSF) through the grant PZ00P2_180112. This work has been completed within the Swiss Competence Center on Energy Research - Supply of Electricity with support of the Innosuisse. The software package Parrot is available upon request to the authors.

A Weak formulation of Biot's equations

A.1 Mathematical preliminaries

We denote by $\mathbb{C}$ the set of complex numbers and by $\mathrm{j} = \sqrt{-1}$ the imaginary unit. For a number $a \in \mathbb{C}$, the symbol a^* will denote the complex conjugate, $\Re\{a\} \in \mathbb{R}$ the real part, and $\Im\{a\} \in \mathbb{R}$ the imaginary part. Given two elements $a, b \in \mathbb{C}$, we introduce the product $(a, b)_{\mathbb{C}} := a\, b^*$ so that the modulus of a can be computed as $|a| = \sqrt{(a, a)_{\mathbb{C}}}$. $\mathbb{V}$ is the complex Euclidean space $\mathbb{C}^d$ provided with the inner product

$$(\underline{u}, \underline{u})_{\mathbb{V}} := \underline{u} \cdot \underline{v}^* = \sum_{i=1}^{d} u_i\, v_i^*, \quad \underline{u}, \underline{v} \in \mathbb{V}. \tag{15}$$

The space of the second-order tensors over $\mathbb{V}$ is denoted by $\mathbb{M}$. Once a basis is introduced over $\mathbb{V}$, the space $\mathbb{M}$ can be identified with $\mathbb{C}^{d\times d}$ and we provide it with the scalar product

$$(\underline{\underline{\sigma}}, \underline{\underline{\tau}})_{\mathbb{M}} := \underline{\underline{\sigma}} : \underline{\underline{\tau}}^* = \sum_{i=1}^{d}\sum_{j=1}^{d} \sigma_{ik}\tau_{ik}^*, \quad \underline{\underline{\sigma}}, \underline{\underline{\tau}} \in \mathbb{M}. \tag{16}$$

For a tensor $\underline{\underline{\sigma}}$, the symbol $\underline{\underline{\sigma}}^H$ denotes the adjoint whose components are $\sigma_{ik}^H = (\sigma_{ki})^*$ and the symbol σ^T denotes the transpose whose components are $\sigma_{ik}^T = \sigma_{ki}$. The symmetric part of a tensor is denoted by

$$\operatorname{sym} \underline{\underline{\sigma}} = \frac{\underline{\underline{\sigma}} + \underline{\underline{\sigma}}^T}{2}, \tag{17}$$

while the Hermitian part is denoted by

$$\operatorname{Herm} \underline{\underline{\sigma}} = \frac{\underline{\underline{\sigma}} + \underline{\underline{\sigma}}^H}{2}. \tag{18}$$

The symbol $\operatorname{tr}(\underline{\underline{\sigma}})$ is the usual trace operator. The operators *, $\Re$, and, $\Im$ are intended to be applied component-wise to a vector or a tensor.

Before deriving the weak formulation of Biot's equations, we first introduce the suitable function spaces. Given a vector space $\mathbb{W}$, which can be $\mathbb{R}$, $\mathbb{C}$, $\mathbb{V}$, or

$\mathbb{M}$, for $p \in [1, \infty)$, we denote with $L^p(\Omega, \mathbb{W})$ the space of p-integrable functions defined on Ω with values in $\mathbb{W}$. The space $L^2(\Omega, \mathbb{W})$ is endowed with the scalar product

$$(p, q)_{L^2(\Omega,\mathbb{W})} := \int_\Omega (p, q)_{\mathbb{W}} \, \mathrm{d}\Omega, \quad p, q \in L^2(\Omega, \mathbb{W}), \tag{19}$$

and the norm

$$\|p\|_{L^2(\Omega,\mathbb{W})} = \sqrt{(p, p)_{L^2(\Omega,\mathbb{W})}}. \tag{20}$$

Instead, $L^\infty(\Omega, W)$ is the space of the essentially bounded functions defined on Ω. The operators ∇ and div are the usual gradient and divergence operators, respectively. They are intended to be applied to the real and the imaginary parts separately. For example, given a function $p : \Omega \to \mathbb{C}$, the gradient is defined as

$$\nabla p = \nabla \Re\{p\} + \mathrm{j} \, \nabla \Im\{p\}. \tag{21}$$

The symmetric gradient of a function $\underline{v} : \Omega \to \mathbb{V}$ is denoted by

$$\underline{\underline{\varepsilon}}(\underline{v}) = \operatorname{sym} \nabla \underline{v} \tag{22}$$

and the following identity holds

$$\operatorname{tr}(\underline{\underline{\varepsilon}}(\underline{v})) = \operatorname{tr}(\nabla \underline{v}) = \underline{\underline{I}} : \nabla \, \underline{v} = \operatorname{div} \underline{v}, \tag{23}$$

where $\underline{\underline{I}}$ is the second order identity tensor. We define the following spaces

$$H^1(\Omega, \mathbb{C}) = \{p \in L^2(\Omega, \mathbb{C}) \,|\, \nabla p \in L^2(\Omega, \mathbb{V})\} \tag{24}$$

and

$$H^1(\Omega, \mathbb{V}) = \{\underline{v} \in L^2(\Omega, \mathbb{V}) \,|\, \nabla \underline{v} \in L^2(\Omega, \mathbb{M})\} \tag{25}$$

endowed with the standard H^1 scalar products. For $\Gamma \subset \partial\Omega$, we denote as

$$H^1_\Gamma(\Omega, \mathbb{W}) = \{w \in H^1(\Omega, \mathbb{W}) \,|\, w|_\Gamma = 0\}. \tag{26}$$

Finally, in order to simplify the notation, we define the following function spaces $V = H^1_{\Gamma^{\mathbf{u}}_D}(\Omega, \mathbb{V})$ and $Q = H^1_{\Gamma^{p}_D}(\Omega, \mathbb{C})$.

A.2 Weak formulation of Biot's equations with periodic boundary conditions

In order to formally derive the weak formulation of the system of equations (1)-(2), we first consider a test function $\underline{v} \in V$, multiply (1) by $\underline{v}^*$, and integrate over Ω

$$\int_\Omega (\operatorname{div} \underline{\underline{\sigma}}) \cdot \underline{v}^* \, \mathrm{d}\Omega = 0. \tag{27}$$

Using Green's formula, we obtain

$$\int_\Omega \underline{\underline{\sigma}} : \nabla \underline{v}^* \, \mathrm{d}\Omega = \sum_{\mathrm{s} \in \{-1,1\}} \sum_{i=1}^{d} \int_{\Gamma^i_{\mathrm{sL}}} \underline{\underline{\sigma}} \, \underline{n} \cdot \underline{v}^* \, \mathrm{d}\Gamma. \tag{28}$$

The symmetry of $\underline{\underline{\sigma}}$ implies that

$$\underline{\underline{\sigma}} : \nabla \underline{v}^* = \underline{\underline{\sigma}} : \underline{\underline{\epsilon}}(\underline{v}^*) \tag{29}$$

and, finally, using the fact that the test functions belong to V and the boundary conditions (7), we observe that the boundary integral at the right-hand side vanishes giving

$$\int_\Omega \underline{\underline{\sigma}} : \boldsymbol{\epsilon}(\underline{v}^*)\, \mathrm{d}\Omega = 0. \tag{30}$$

Similarly, for (2), we consider a test function $q \in Q$. Multiplying this equation by q^* and integrating over Ω, we obtain

$$-\,\mathrm{j} \int_\Omega \alpha\, \mathrm{div}\, \underline{u}\, q^* \mathrm{d}\Omega - \mathrm{j} \int_\Omega \frac{p}{M} q^* \mathrm{d}\Omega + \frac{1}{\omega} \int_\Omega \mathrm{div} \left(\frac{k}{\eta} \nabla p \right) q^* \mathrm{d}\Omega = 0. \tag{31}$$

Applying again Green's formula, the last term becomes

$$-\int_\Omega \left(\frac{k}{\eta} \nabla p \right) \cdot \nabla q^* \mathrm{d}\Omega + \sum_{\mathrm{s} \in \{-1,1\}} \sum_{i=1}^{d} \int_{\Gamma^i_{\mathrm{sL}}} \frac{k}{\eta} \nabla p \cdot \underline{n}\, q^*|_{\Gamma^i_{\mathrm{sL}}}\, \mathrm{d}\Gamma. \tag{32}$$

As for the linear momentum equation, the boundary integral vanishes and we obtain

$$-\,\mathrm{j} \int_\Omega \alpha\, \mathrm{div}\, \underline{u}\, q^* \mathrm{d}\Omega - \mathrm{j} \int_\Omega \frac{1}{M} p q^* \mathrm{d}\Omega - \frac{1}{\omega} \int_\Omega \frac{k}{\eta} \nabla p \cdot \nabla q^*\, \mathrm{d}\Omega = 0. \tag{33}$$

In order to include the Dirichlet boundary conditions on the displacement, we define the set

$$U = \{ \underline{v} \in H^1(\Omega, \mathbb{V}) \,|\, \underline{v}|_{\Gamma^i_{\mathrm{L}}} - \underline{v}|_{\Gamma^i_{-\mathrm{L}}} = \underline{\alpha}_i \quad \text{with } i = 1, \ldots, d \}. \tag{34}$$

Hence, exploiting the definition of stress (4), the weak formulation of Biot's equation can be written as:
Find $(\underline{u}, p) \in U \times Q$ such that

$$\begin{array}{rcrcll} a(\underline{u}, \underline{v}) & - & b(\underline{v}^*, p^*) & = & 0 & \forall \underline{v} \in V, \\ - \;\; \mathrm{j}\, b(\underline{u}, q) & - & d(p, q) & = & 0 & \forall q \in Q, \end{array} \tag{35}$$

where

$$\begin{array}{rcl} a(\underline{u}, \underline{v}) & = & \int_\Omega 2\mu \boldsymbol{\epsilon}(\underline{u}) : \boldsymbol{\epsilon}(\underline{v}^*) + \lambda\, \mathrm{div}\, \underline{u}\, \mathrm{div}\, \underline{v}^*\, \mathrm{d}\Omega, \\ b(\underline{u}, q) & = & \int_\Omega \alpha\, \mathrm{div}\, \underline{u}\, q^*\, \mathrm{d}\Omega, \\ d(p, q) & = & \mathrm{j}\; m(p, q) + c(p, q), \\ m(p, q) & = & \int_\Omega \frac{1}{M} p\, q^* \mathrm{d}\Omega, \\ c(p, q) & = & \int_\Omega \frac{k}{\eta} \nabla p \cdot \nabla q^* \mathrm{d}\Omega. \end{array} \tag{36}$$

In (35), the right-hand side is null since we assume no external force is acting on the REV. The external loads are encoded in the essential boundary

conditions in the set U. In order to formally express these boundary conditions, the displacement can be written as

$$\underline{u} = \underline{u}_0 + \underline{u}_{\boldsymbol{\alpha}}, \tag{37}$$

where $\underline{u}_0$ belongs to V and $\underline{u}_{\boldsymbol{\alpha}}$ is a lifting function, which can be any element in U. Hence, for a given $\underline{u}_{\boldsymbol{\alpha}}$, the problem (35) can be written as:
Find $(\mathbf{u}_0, p) \in V \times Q$ such that

$$\begin{array}{rcccccll} a(\underline{u}_0, \underline{v}) & - & b(\underline{v}^*, p^*) & = & -a(\underline{u}_{\boldsymbol{\alpha}}, \underline{v}) & & \forall \underline{v} \in V, \\ - \ \mathrm{j}\ b(\underline{u}_0, q) & - & d(p, q) & = & \mathrm{j}\ b(\underline{u}_{\boldsymbol{\alpha}}, q) & & \forall q \in Q. \end{array} \tag{38}$$

The solution can then be computed from (37). Finally, we also observe that $\underline{u}_0$ is defined up to a constant vector, since for any constant $\underline{c}$, $(\underline{u}_0 + \underline{c}, p)$ is also solution of (38). In order to eliminate this ambiguity, the space V can be replaced with

$$V_0 = \left\{ \underline{v} \in V \ : \ \int_\Omega \underline{v} \, \mathrm{d}\Omega = \underline{0} \right\}. \tag{39}$$

A.3 Properties of bilinear forms

The analysis of problem (38) is not trivial. Similar problems on real function spaces have been considered in [12]. Here, we limit ourselves to prove two properties that are useful for the analysis of the discrete problem.

While for Hermitian complex bilinear forms, the proof of coercivity is just a simple extension of the real case, it needs to be generalized for non-Hermitian bilinear forms [45]. In particular, we say that a bilinear form $c(\,\cdot\,,\,\cdot\,)$ defined over a complex Hilbert space Q is $\mathbb{C}$-coercive, if there exists a constant γ such that $|c(p,p)| > \gamma \|p\|_Q^2$ for all $p \in Q$.

Property A.1 *The bilinear form $a(\,\cdot\,,\,\cdot\,)$ is coercive over V_0 with coercivity constant*

$$\alpha = \min(\mu_b, \mu_f), \tag{40}$$

where μ is the shear modulus. This can be seen observing that $a(\underline{u}, \underline{u}) = a(\Re\underline{u}, \Re\underline{u}) + a(\Im\underline{u}, \Im\underline{u})$. Applying Korn's inequality to both bilinear forms at the right-hand side, coercivity can be easily proven [9].

Property A.2 *The bilinear form $d(\,\cdot\,,\,\cdot\,)$ is $\mathbb{C}$-corcive over Q, with coercivity constant $\delta = \frac{1}{2}\min(\frac{c_0}{\omega}, m_0)$, where*

$$c_0 = \min(k_b/\eta_b, k_f/\eta_f) \ \textit{and} \ m_0 = \min(1/M_b, 1/M_f).$$

We observe that

$$|d(u,u)| \geq \Re\, d(p,p) = \frac{1}{\omega}\int_\Omega \frac{k}{\eta} \nabla p \cdot \nabla p \, \mathrm{d}\Omega \geq \frac{1}{\omega}\min(k_b/\eta_b, k_f/\eta_f) \|\nabla p\|^2_{L^2(\Omega,\mathbb{V})} \tag{41}$$

and

$$|d(u,u)| \geq \Im\, d(u,u) = \int_\Omega \frac{1}{M}\, p^2 \,\mathrm{d}\Omega \geq \min(1/M_b, 1/M_f)\|p\|^2_{L^2(\Omega,\mathbb{C})}. \tag{42}$$

Summing up (41) and (42), we obtain

$$|d(p,p)| \geq \frac{1}{2}\min(m_0, \frac{c_0}{\omega})\|p\|^2_V. \tag{43}$$

B Finite element discretization of Biot's equations

Let $\mathcal{T}$ be a 1-irregular triangulation of Ω. We denote by $\mathbb{Q}_1$ the space of real bilinear functions for $d = 2$ and of real trilinear functions for $d = 3$. We define the conforming interpolation spaces over $\mathcal{T}$

$$X_\mathcal{T} = \{p_h \in C^0(\Omega, \mathbb{R}) \,:\, p_h|_K \in \mathbb{Q}_1 \,\forall K \in \mathcal{T}\} \tag{44}$$

and

$$Y_\mathcal{T} = \{\underline{u}_h \in C^0(\Omega, \mathbb{R}^d) \,:\, (\underline{u}_h)_i|_K \in \mathbb{Q}_1 \,\forall K \in \mathcal{T} \text{ and } i = 1, \ldots, d\}. \tag{45}$$

The dimension of the space $X_\mathcal{T}$ is N^r and the dimension of the space $Y_\mathcal{T}$ is dN^r. In order to include boundary conditions in the interpolation spaces above, we define $V_\mathcal{T} = Y_\mathcal{T} \cap V$, and $Q_\mathcal{T} = X_\mathcal{T} \cap Q$. For any $\underline{u}_{\boldsymbol{\alpha}}$, the FE approximation of problem (38) has the following form:

Find $(\underline{u}_{0h}, p_h) \in V_\mathcal{T} \times Q_\mathcal{T}$ such that

$$\begin{array}{rcrcll} a(\underline{u}_{0h}, \underline{v}_h) & - & b(\underline{v}^*_h, p^*_h) & = & -a(\underline{u}_{\boldsymbol{\alpha}}, \underline{v}_h) & \forall \underline{v}_h \in V_\mathcal{T}, \\ - \;\mathrm{j}\, b(\underline{u}_{0h}, q_h) & - & d(p_h, q_h) & = & \mathrm{j}\; b(\underline{u}_{\boldsymbol{\alpha}}, q_h) & \forall q_h \in Q_\mathcal{T}. \end{array} \tag{46}$$

B.1 Uniqueness of the solution of the discretized of Biot's equations

In order to prove the uniqueness of solution of problem (46), we first rewrite it in an algebraic form by introducing the basis functions $\{\Phi_j \in V_\mathcal{T}\}$ and $\{\phi_l \in Q_\mathcal{T}\}$ of $V_\mathcal{T}$ and $Q_\mathcal{T}$, respectively. Expanding the two components of the solution with respect to the basis functions, we obtain the following block linear system

$$\left|\begin{array}{cc} \mathbf{A} & -\mathbf{B}^T \\ -\,\mathrm{j}\,\mathbf{B} & -\mathbf{D} \end{array}\right| \left|\begin{array}{c} \mathbf{u} \\ \mathbf{p} \end{array}\right| = \left|\begin{array}{c} \mathbf{f} \\ \mathbf{g} \end{array}\right|, \tag{47}$$

where $\mathbf{A} \in \mathbb{R}^{dN^r_h \times dN^r_h}$, $\mathbf{B} \in \mathbb{R}^{N^r_h \times dN^r_h}$, and $\mathbf{D} \in \mathbb{C}^{N^r_h \times N^r_h}$ are the matrices related to the bilinear forms a, b, and d, respectively. The elements of such matrices are given by $A_{ij} = a(\Phi_j, \Phi_i)$, $B_{kj} = b(\Phi_j, \phi_k)$, and $D_{kl} = d(\phi_l, \phi_k)$. The vectors $\mathbf{u} \in \mathbb{C}^{dN^r_h}$ and $\mathbf{p} \in \mathbb{C}^{N^r_h}$ are the vectors collecting the unknown

Lagrange coefficients of the discrete displacement and pressure, respectively. The two vectors at the right-hand side are defined as $F_i = -a(\mathbf{u}_{\boldsymbol{\alpha}}, \Phi_i)$ and $G_k = j\, b(\mathbf{u}_{\boldsymbol{\alpha}}, \phi_k)$. The matrix $\mathbf{D}$ can be written as $\mathbf{D} = \frac{1}{\omega}\mathbf{C} + \mathrm{j}\,\mathbf{M}$.

The stiffness matrix in the linear system (47) is indefinite and we show that it is invertible thanks to from properties A.1 and A.2. First, owing to property A.1, $\mathbf{A}$ is Hermitian and semi-positive definite, having in its kernel the displacements associated to rigid body motions. Hence, $\mathbf{u}$ can be formally computed from

$$\mathbf{u} = \mathbf{A}^{-1}(\mathbf{F} + \mathbf{B}^T\mathbf{p}), \tag{48}$$

where $\mathbf{u}$ is defined up to a vector in the kernel of $\mathbf{A}$.

Replacing this equation in the second line of (47), we obtain

$$\mathbf{S}\mathbf{p} = -\,\mathrm{j}\,\mathbf{B}\mathbf{A}^{-1}\mathbf{f} - \mathbf{g}, \tag{49}$$

where $\mathbf{S} = \mathbf{D} + \mathrm{j}\,\mathbf{B}\mathbf{A}^{-1}\mathbf{B}^T$. Before proving that $\mathbf{S}$ is invertible, we observe that $\mathbf{B}\mathbf{A}^{-1}\mathbf{B}^T$ is symmetric and semi-positive definite and $\mathbf{M}$, being a scaled mass matrix, is symmetric and positive definite.

Property B.1 *The matrix* $\mathbf{S}$ *is regular.*

Let us suppose by contradiction that $\mathbf{S}$ is not regular. This means there exists a non-trivial vector $\mathbf{r}$ associated to a function $r_h \in Q_{\mathcal{T}}$, such that $\mathbf{S}\mathbf{r} = \mathbf{0}$. Hence, by definition of $\mathbf{S}$, we obtain

$$\begin{aligned} 0 = |\mathbf{r}^T\mathbf{S}\mathbf{r}| = |\frac{1}{\omega}\mathbf{r}^T\mathbf{C}\mathbf{r} + \mathrm{j}\,\mathbf{r}^T(\mathbf{M} + \mathbf{B}\mathbf{A}^{-1}\mathbf{B}^T)\mathbf{r}| > \\ \frac{1}{2}|\frac{1}{\omega}\mathbf{r}^T\mathbf{C}\mathbf{r}| + \frac{1}{2}|\mathbf{r}^T(\mathbf{M} + \mathbf{B}\mathbf{A}^{-1}\mathbf{B}^T)\mathbf{r}| > \\ \frac{1}{2}|\frac{1}{\omega}\mathbf{r}^T\mathbf{C}\mathbf{r}| + \frac{1}{2}|\mathbf{r}^T\mathbf{M}\mathbf{r}| > \\ \frac{1}{2}|\mathbf{r}^T\mathbf{D}\mathbf{r}| = \frac{1}{2}|d(r_h, r_h)|. \end{aligned} \tag{50}$$

Therefore, property (A.2) leads to a contradiction

$$0 = |\mathbf{r}^T\mathbf{S}\mathbf{r}| > \frac{1}{2}\delta\|r_h\|_Q^2 > 0,$$

which proves the invertibility of $\mathbf{S}$. This ensures the uniqueness of $\mathbf{p}$, while equation (48) ensures that of $\mathbf{u}$. The uniqueness of $\mathbf{p}$ ensures that the FE problem (46) does not present spurious modes.

References

[1] Amestoy, P.R., Duff, I.S., L'excellent, J.Y.: Multifrontal parallel distributed symmetric and unsymmetric solvers. Computer methods in applied mechanics and engineering **184**(2-4), 501–520 (2000)

[2] Bangerth, W., Hartmann, R., Kanschat, G.: deal.ii – a general-purpose object-oriented finite element library. ACM Transactions on Mathematical Software (TOMS) **33**(4), 24 (2007)

[3] Berger, M.J., Colella, P.: Local adaptive mesh refinement for shock hydrodynamics. Journal of computational Physics **82**(1), 64–84 (1989)

[4] Bielak, J., Ghattas, O., Kim, E.: Parallel octree-based finite element method for large-scale earthquake ground motion simulation. Computer Modeling in Engineering and Sciences **10**(2), 99 (2005)

[5] Biot, M.A.: General theory for three-dimensional consolidation. Journal of Applied Physics **12**, 155–164 (1941)

[6] Biot, M.A.: Theory of propagation of elastic waves in a fluid-saturated porous solid. I. Low frequency range. Journal of the Acoustical Society of America **28**, 168–178 (1956)

[7] Biot, M.A.: Theory of propagation of elastic waves in a fluid-saturated porous solid. II. High frequency range. Journal of the Acoustical Society of America **28**, 179–191 (1956)

[8] Biot, M.A.: Mechanics of deformation and acoustic propagation in porous media. Journal of Applied Physics **33**, 1482–1498 (1962)

[9] Bochev, P., Lehoucq, R.: Energy principles and finite element methods for pure traction linear elasticity. Computational Methods in Applied Mathematics Comput. Methods Appl. Math. **11**(2), 173–191 (2011)

[10] Boffi, D.: On the finite element method on quadrilateral meshes. Applied numerical mathematics **56**(10-11), 1271–1282 (2006)

[11] Bourbié, T., Coussy, O., Zinszner, B.: Acoustics of porous media. Editions Technip (1987)

[12] Brezzi, F., Fortin, M.: Mixed and Hybrid Finite Element Methods. Springer-Verlag New York, Inc., New York, NY, USA (1991)

[13] Brezzi, F., Pitkäranta, J.: On the stabilization of finite element approximations of the Stokes equations. In: Efficient Solutions of Elliptic Systems, pp. 11–19. Springer (1984)

[14] Brown, J.D., Lowe, L.L.: Multigrid elliptic equation solver with adaptive mesh refinement. Journal of Computational Physics **209**(2), 582–598 (2005)

[15] Burstedde, C., Wilcox, L.C., Ghattas, O.: p4est: Scalable algorithms for parallel adaptive mesh refinement on forests of octrees. SIAM Journal on Scientific Computing **33**(3), 1103–1133 (2011)

[16] Carcione, J.M., Helle, H.B., Pham, N.H.: White's model for wave propagation in partially saturated rocks: Comparison with poroelastic numerical experiments. Geophysics **68**, 1389–1398 (2003)

[17] Carcione, J.M., Quiroga-Goode, G.: Some aspects of the physics and numerical modeling of Biot compressional waves. Journal of Computational Acoustics **3**, 261–280 (1995)

[18] Carstensen, C., Hu, J.: Hanging nodes in the unifying theory of a posteriori finite element error control. Journal of Computational Mathematics **27**(2/3), 215–236 (2009). URL http://www.jstor.org/stable/43693503

[19] Carstensen, C., Hu, J., Orlando, A.: Framework for the a posteriori error analysis of nonconforming finite elements. SIAM Journal on Numerical Analysis **45**(1), 68–82 (2007). URL http://www.jstor.org/stable/40232918

[20] Dörfler, W.: A convergent adaptive algorithm for Poisson's equation. SIAM Journal on Numerical Analysis **33**(3), 1106–1124 (1996)

[21] de Dreuzy, J.R., Davy, P., Bour, O.: Hydraulic properties of two-dimensional random fracture networks following a power law length distribution: 1. Effective connectivity. Water Resources Research **37**, 2065–2078 (2001)

[22] Düster, A., Parvizian, J., Yang, Z., Rank, E.: The finite cell method for three-dimensional problems of solid mechanics. Computer Methods in Applied Mechanics and Engineering **197**(45), 3768 – 3782 (2008). DOI https://doi.org/10.1016/j.cma.2008.02.036. URL http://www.sciencedirect.com/science/article/pii/S0045782508001163

[23] Ern, A., Meunier, S.: A posteriori error analysis of euler-galerkin approximations to coupled elliptic-parabolic problems. ESAIM: Mathematical Modelling and Numerical Analysis **43**(2), 353–375 (2009)

[24] Favino, M., Grillo, A., Krause, R.: A stability condition for the numerical simulation of poroelastic systems. In: Poromechanics V: Proceedings of the Fifth Biot Conference on Poromechanics, pp. 919–928 (2013)

[25] Favino, M., Hunziker, J., Holliger, K., Krause, R.: An Accuracy Condition for the Finite Element Discretization of Biot's Equations on Triangular Meshes. In: Poromechanics VI, pp. 172–181 (2017)

[26] Gaston, D., Newman, C., Hansen, G., Lebrun-Grandie, D.: Moose: A parallel computational framework for coupled systems of nonlinear equations. Nuclear Engineering and Design **239**(10), 1768–1778 (2009)

[27] Griebel, M., Scherer, K., Schweitzer, M.: Robust norm equivalencies for diffusion problems. Mathematics of computation **76**(259), 1141–1161 (2007)

[28] Hou, T.Y., Wu, X.H.: A multiscale finite element method for elliptic problems in composite materials and porous media. Journal of computational physics **134**(1), 169–189 (1997)

[29] Hunziker, J., Favino, M., Caspari, E., Quintal, B., Rubino, J.G., Krause, R., Holliger, K.: Seismic attenuation in realistic fracture networks. Proceedings of the 6th Biot Conference on Poromechanics (2017)

[30] Hunziker, J., Favino, M., Caspari, E., Quintal, B., Rubino, J.G., Krause, R., Holliger, K.: Seismic attenuation and stiffness modulus dispersion in porous rocks containing stochastic fracture networks. Journal of Geophysical Research (2018)

[31] Jänicke, R., Quintal, B., Steeb, H.: Numerical homogenization of mesoscopic loss in poroelastic media. European Journal of Mechanics A/Solids **49**, 382–395 (2015)

[32] Johnson, D.L.: Theory of frequency dependent acoustics in patchy-saturated porous media. Journal of the Acoustical Society of America **110**, 682–694 (2001)

[33] Kirk, B.S., Peterson, J.W., Stogner, R.H., Carey, G.F.: libmesh: a c++ library for parallel adaptive mesh refinement/coarsening simulations. Engineering with Computers **22**(3-4), 237–254 (2006)

[34] Kornhuber, R., Krause, R.: Adaptive multigrid methods for signorini's problem in linear elasticity. Computing and Visualization in Science **4**(1), 9–20 (2001). DOI 10.1007/s007910100052. URL https://doi.org/10.1007/s007910100052

[35] Krzikalla, F., Müller, T.M.: Anisotropic P-SV-wave dispersion and attenuation due to inter-layer flow in thinly layered porous rocks. Geophysics **76**, WA135–WA145 (2011)

[36] Kuteynikova, M., Tisato, N., Jänicke, R., Quintal, B.: Numerical modeling and laboratory measurements of seismic attenuation in partially saturated rock. Geophysics **79**, L13–L20 (2014)

[37] Lambert, G., Gurevich, B., Brajanovski, M.: Attenuation and dispersion of P-waves in porous rocks with planar fractures: Comparison of theory and numerical simulations. Geophysics **71**, N41–N45 (2006)

[38] Li, S., Xu, Z., Ma, G., Yang, W.: An adaptive mesh refinement method for a medium with discrete fracture network: The enriched persson?s method. Finite Elements in Analysis and Design **86**, 41–50 (2014)

[39] Masson, Y.J., Pride, S.R.: Poroelastic finite difference modeling of seismic attenuation and dispersion due to mesoscopic-scale heterogeneity. Journal of Geophysical Research **112**, B03204 (2007)

[40] Masson, Y.J., Pride, S.R.: Seismic attenuation due to patchy saturation. Journal of Geophysical Research **116**, B03206 (2011)

[41] Mavko, G., Mukerji, T., Dvorkin, J.: The Rock Physics Handbook, Second Edition. Cambridge University Press (2009)

[42] Mavko, G., Mukerji, T., Dvorkin, J.: The rock physics handbook: Tools for seismic analysis of porous media. Cambridge university press (2009)

[43] Müller, T.M., Gurevich, B., Lebedev, M.: Seismic wave attenuation and dispersion resulting from wave-induced flow in porous rocks - A review. Geophysics **75**, 75A147–75A164 (2010)

[44] Norris, A.N.: Low-frequency dispersion and attenuation in partially saturated rocks. Journal of the Acoustical Society of America **94**, 359–370 (1993)

[45] Oden, J.T., Demkowicz, L.: Applied functional analysis. CRC press (2010)

[46] Odsæter, L.H., Kvamsdal, T., Larson, M.G.: A simple embedded discrete fracture–matrix model for a coupled flow and transport problem in porous media. Computer Methods in Applied Mechanics and Engineering **343**, 572–601 (2019)

[47] Pride, S.R., Berryman, J.G., Harris, J.M.: Seismic attenuation due to wave-induced flow. Journal of Geophysical Research **109**, B01201 (2004)

[48] Quintal, B., Jänicke, R., Rubino, J.G., Steeb, H., Holliger, K.: Sensitivity of S-wave attenuation to the connectivity of fractures in fluid-saturated rocks. Geophysics **79**, WB15–WB24 (2014)

[49] Quintal, B., Steeb, H., Frehner, M., Schmalholz, S.M.: Quasi-static finite element modeling of seismic attenuation and dispersion due to wave-induced fluid flow in poroelastic media. Journal of Geophysical Research **116**, B01201 (2011)

[50] Riedlbeck, R., Pietro, D.A.D., Ern, A., Granet, S., Kazymyrenko, K.: Stress and flux reconstruction in biot's poro-elasticity problem with application to a posteriori error analysis. Computers & Mathematics with Applications **73**(7), 1593 – 1610 (2017). DOI https://doi.org/10.1016/j.camwa.2017.02.005

[51] Rubino, J.G., Caspari, E., Müller, T.M., Milani, M., Barbosa, N.D., Holliger, K.: Numerical upscaling in 2-D heterogeneous poroelastic rocks: Anisotropic attenuation and dispersion of seismic waves. Journal of Geophysical Research: Solid Earth **121**, 6698–6721 (2016)

[52] Rubino, J.G., Guarracino, L., Müller, T.M., Holliger, K.: Do seismic waves sense fracture connectivity? Geophysical Research Letters **40**, 692–696 (2013)

[53] Rubino, J.G., Ravazzoli, C.L., Santos, J.E.: Equivalent viscoelastic solids for heterogeneous fluid-saturated porous rocks. Geophysics **74**, N1–N13 (2009)

[54] Sampath, R.S., Biros, G.: A parallel geometric multigrid method for finite elements on octree meshes. SIAM Journal on Scientific Computing **32**(3), 1361–1392 (2010)

[55] Sarkis, M.: Partition of unity coarse spaces: enhanced versions, discontinuous coefficients and applications to elasticity. Domain decomposition methods in science and engineering pp. 149–158 (2003)

[56] Sauter, S.A., Warnke, R.: Composite finite elements for elliptic boundary value problems with discontinuous coefficients. Computing **77**(1), 29–55 (2006)

[57] Walloth, M., Krause, R.: Adaptive numerical simulation of dynamic contact problems. In: A. Abdulle, S. Deparis, D. Kressner, F. Nobile, M. Picasso (eds.) Numerical Mathematics and Advanced Applications - ENUMATH 2013, pp. 273–281. Springer International Publishing, Cham (2015)

[58] Wang, H.F.: Theory of linear poroelasticity with applications to geomechanics and hydrogeology. Princeton University Press (2017)

[59] White, J.E.: Computed seismic speeds and attenuation in rocks with partial gas saturation. Geophysics **40**, 224–232 (1975)

[60] White, J.E., Mikhaylova, N.G., Lyakhovitskiy, F.M.: Low-frequency seismic waves in fluid-saturated layered rocks. Izvestija Academy of Sciences USSR **11**, 654–659 (1975)

[61] Young, D.P., Melvin, R.G., Bieterman, M.B., Johnson, F.T., Samant, S.S., Bussoletti, J.E.: A locally refined rectangular grid finite element method: application to computational fluid dynamics and computational physics. Journal of Computational Physics **92**(1), 1–66 (1991)

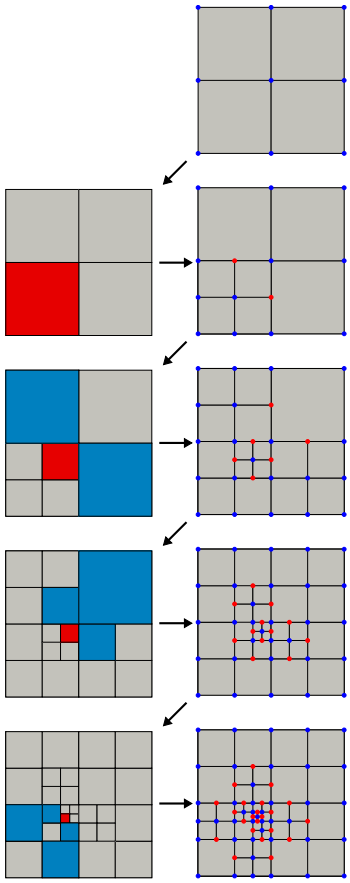

Figure 1: Examples of 1-irregular meshes. Right column, top to bottom: initial mesh and the resulting adapted meshes after one, two, three, and four red-refinement steps. The hanging nodes are colored in red, while regular nodes are colored in blue. Left column: element marked for refinement (red) and elements that have been marked for refinement to keep the resulting mesh 1-irregular (blue).

Step 1
for *each element* K_j *in* $\mathcal{T}_{\ell-1}$ **do**
  for *each fracture* b_i *in* $\mathcal{B}$ **do**
    if *the intersection between* K_j *and* ∂f_j *is non-empty* **then**
      K_j is added to $\mathcal{A}_{\ell-1}$
    end
  end
end
Step 2
repeat
  for *each element* K_j *in* $\mathcal{A}_{\ell-1}$ **do**
    for *each element* K_i *in* $\mathcal{T}_{\ell-1} \backslash \mathcal{A}_{\ell-1}$ **do**
      if *the intersection between* K_j *and* K_i *is non-empty and* $E(K_j) > E(K_i)$ **then**
        K_i is added to $\mathcal{A}_{\ell-1}$
      end
    end
  end
until *the cardinality of* $\mathcal{A}_{\ell-1}$ *is unchanged*;
Step 3
Result: Apply red-refinement to all elements in $\mathcal{A}_{\ell-1}$ to obtain $\mathcal{T}_\ell$

Figure 2: Algorithm of the proposed AMR method for level ℓ.

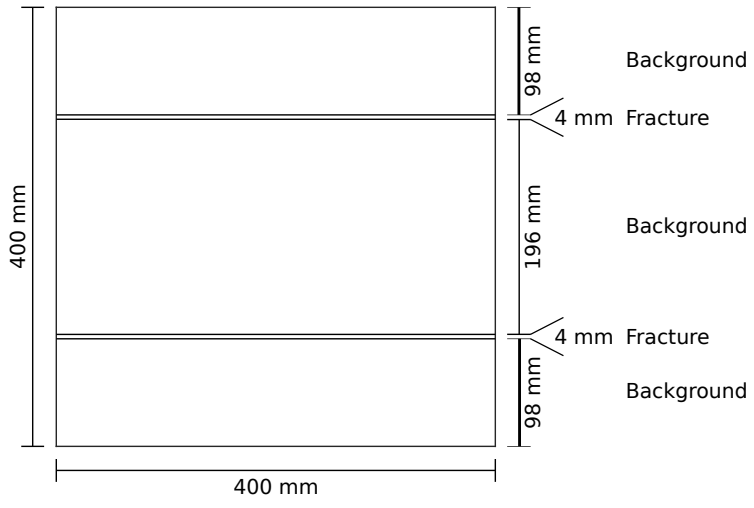

Figure 3: Geometry of the horizontally layered medium considered in example 1. The corresponding material properties are given in Table 1.

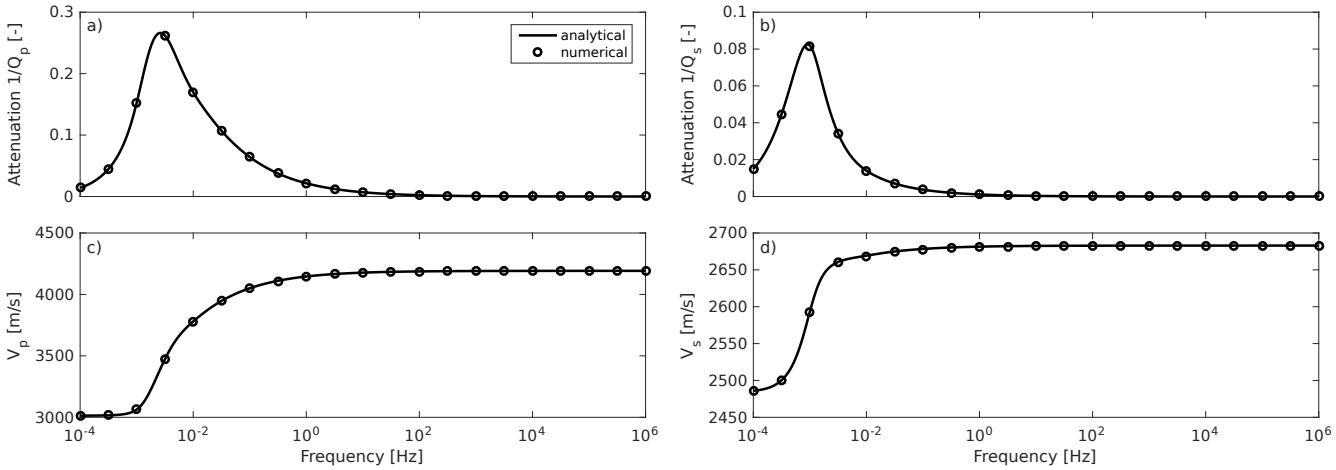

Figure 4: Analytically (solid black line) and numerically (circles) determined attenuation and velocity dispersion at an incidence angle of 30° for a periodically layered medium consisting of two horizontal layers whose material propoerties are given in Table 1. (a) P-wave attenuation, (b) S-wave attenuation, (c) P-wave velocity dispersion, (d) S-wave velocity dispersion. The numerical results correspond to the scenario of fractures resolved by mesh and obtained after 1 AMR level.

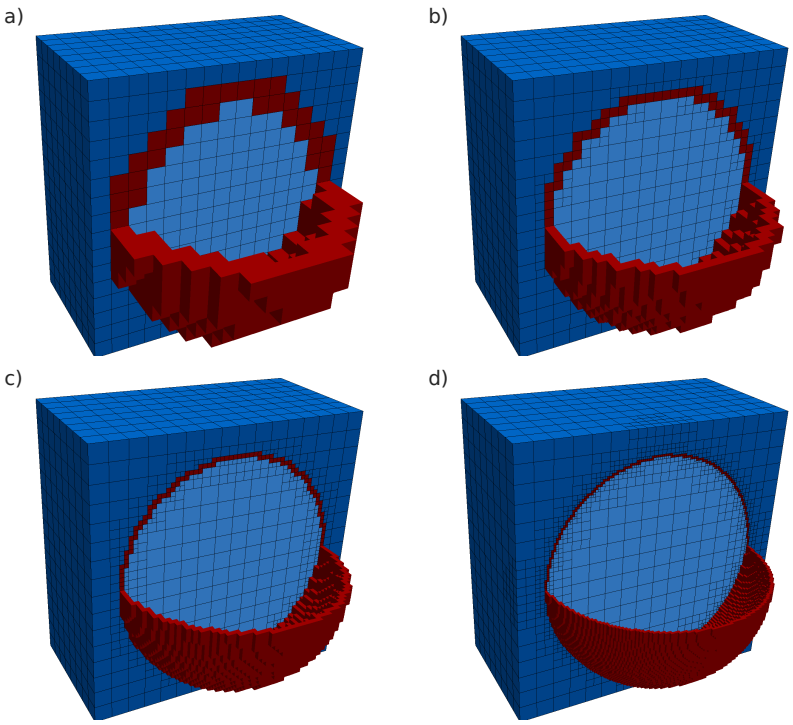

Figure 5: Model consisting of a water-saturated (light blue) spherical porous medium enclosed in a gas-saturated (dark blue) porous background (Table 3). (a) Initial mesh and (b-d) the first three refinement steps. The red elements intersect the boundary of the enclosed sphere and are refined in the subsequent level. Only half of the model is depicted to better visualize the refinement along the boundary of the sphere.

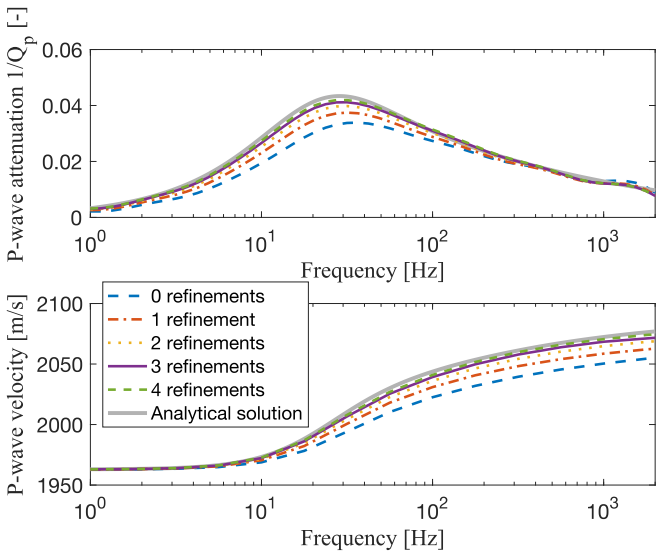

Figure 6: Seismic attenuation and velocity dispersion characteristics at vertical incidence for model shown in Figure 5: analytical solution (bold grey line) and 5 adaptive refinement levels (colored lines).

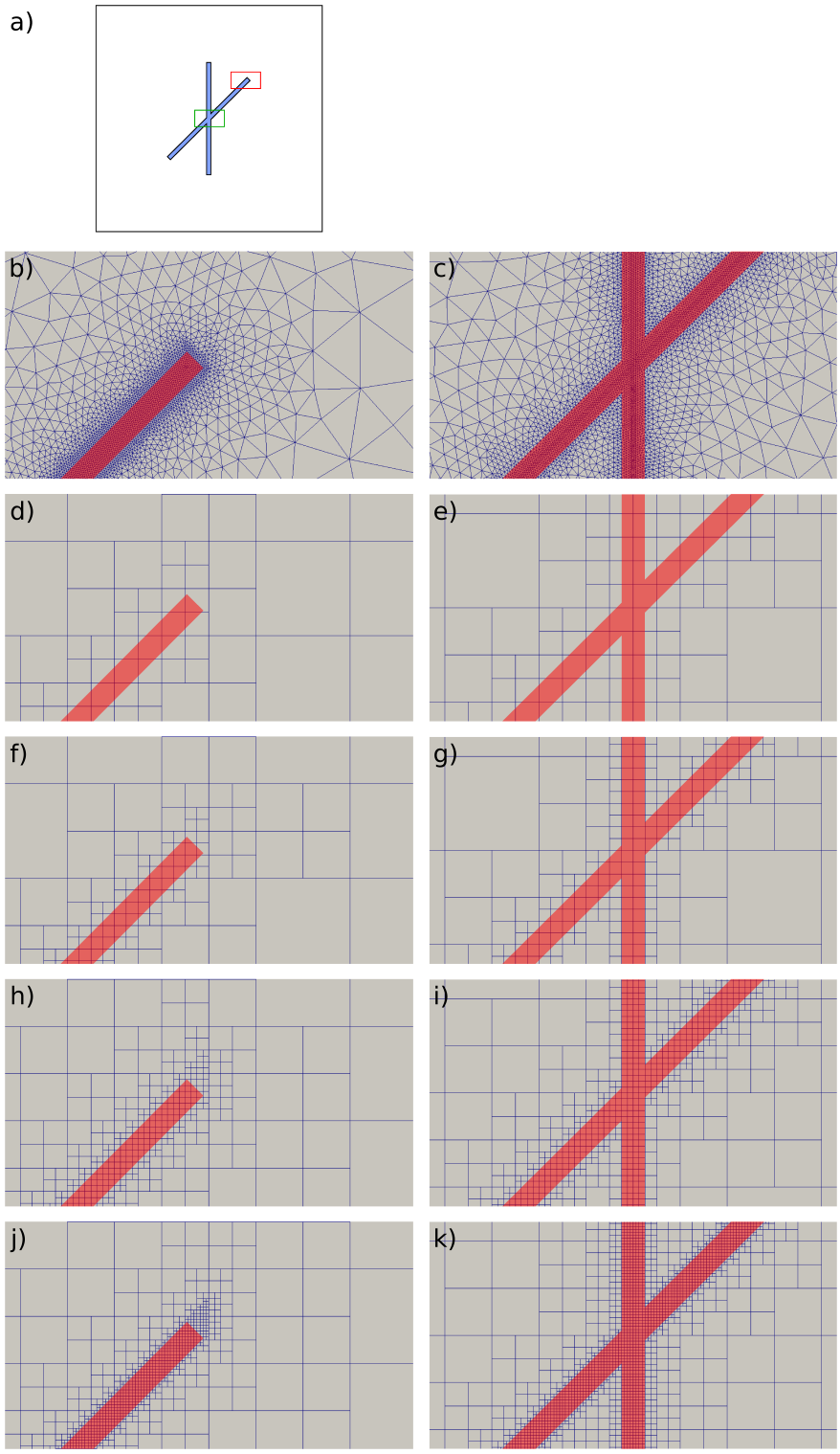

Figure 7: (a) Model containing two fractures (blue) intersecting each other at an angle of 45°. The red rectangle denotes the fracture tip, for which blowups are shown on the left. The green rectangle denotes the crossing of the two fractures, for which corresponding blowups are shown on the right. (b),(c) Triangular mesh following the geometry of the fracture. (d) to (k) Automatically refined meshes created at steps 3, 4, 5, and 6 of the AMR method. The semi-transparent red area indicates the location of the fractures.

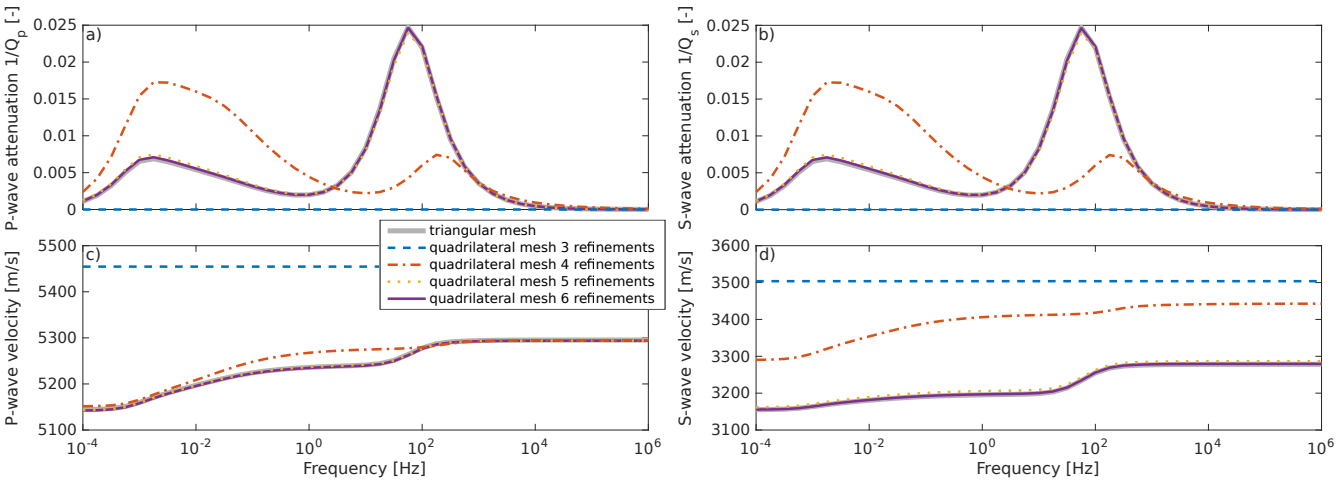

Figure 8: Seismic attenuation and velocity dispersion at vertical incidence for model shown in Figure 7 based on a mesh that explicitly resolves the geometry of the fractures using triangular elements (bold gray curve) and one consisting of quadrilateral elements that is 3 to 6 times adaptively refined in the vicinity of the fractures (colored dashed lines). (a) P-wave attenuation, (b) S-wave attenuation, (c) P-wave velocity dispersion, (d) S-wave velocity dispersion.

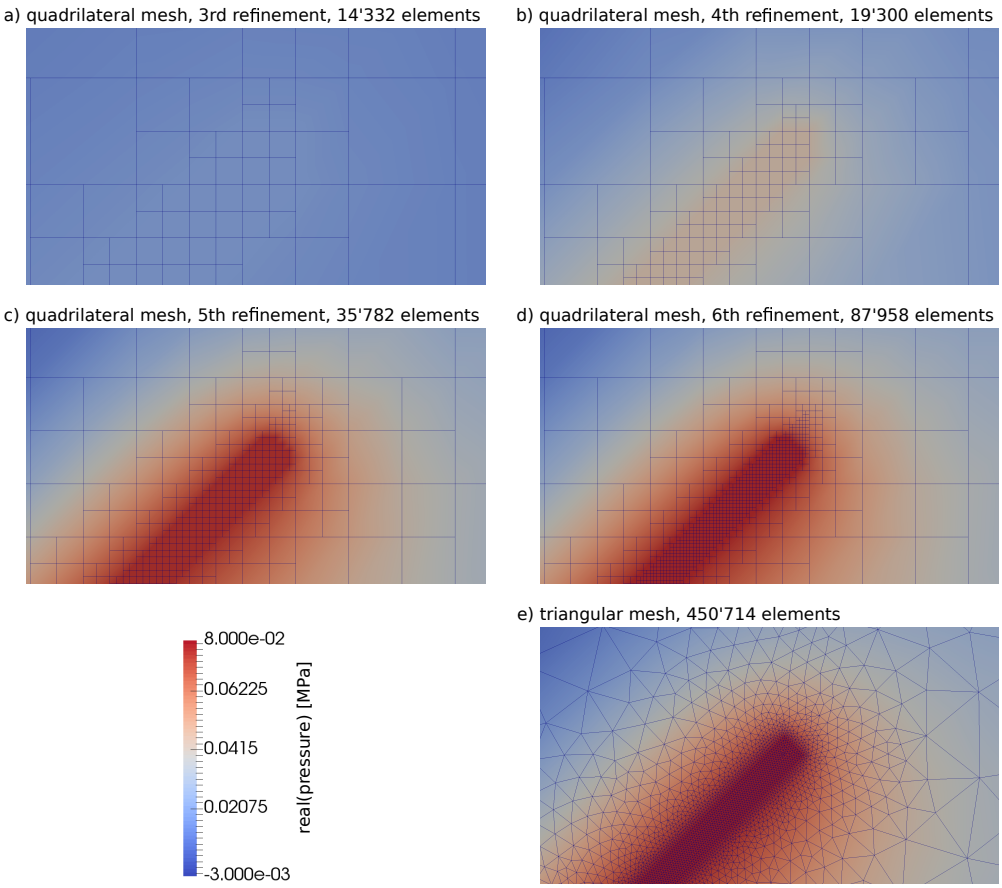

Figure 9: Distribution of real component of the pore fluid pressure at a frequency of 1 Hz in the region blown up in Figure 7. a) - d) Results obtained at steps 3-6 of the AMR method. e) Results obtained with a triangular mesh. Please note the much larger number of triangular mesh elements as compared to the AMR method.

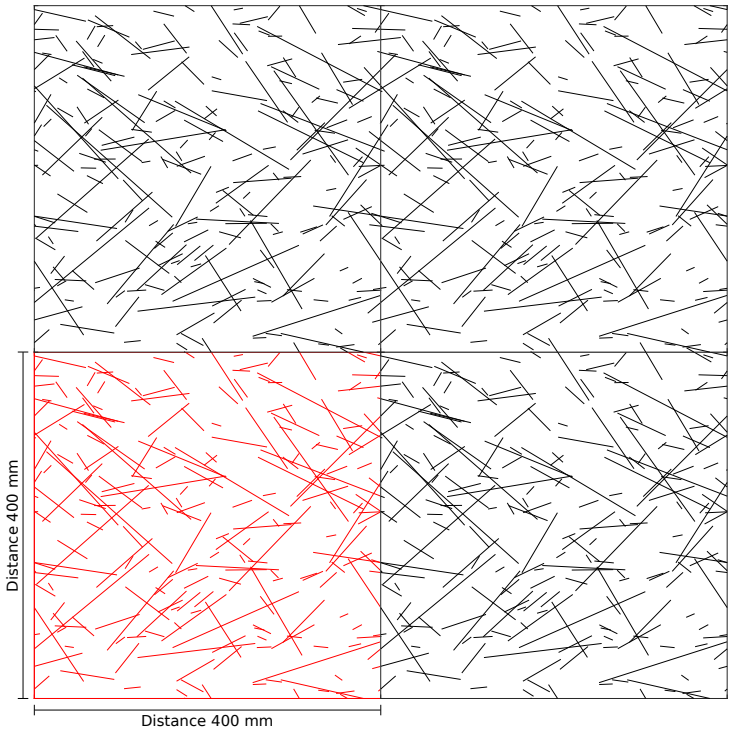

Figure 10: REV of the stochastic fracture network example employed to evaluate the accuracy of the proposed AMR method (red), which has been repeated three times (black) to illustrate the periodicity of the fractures.

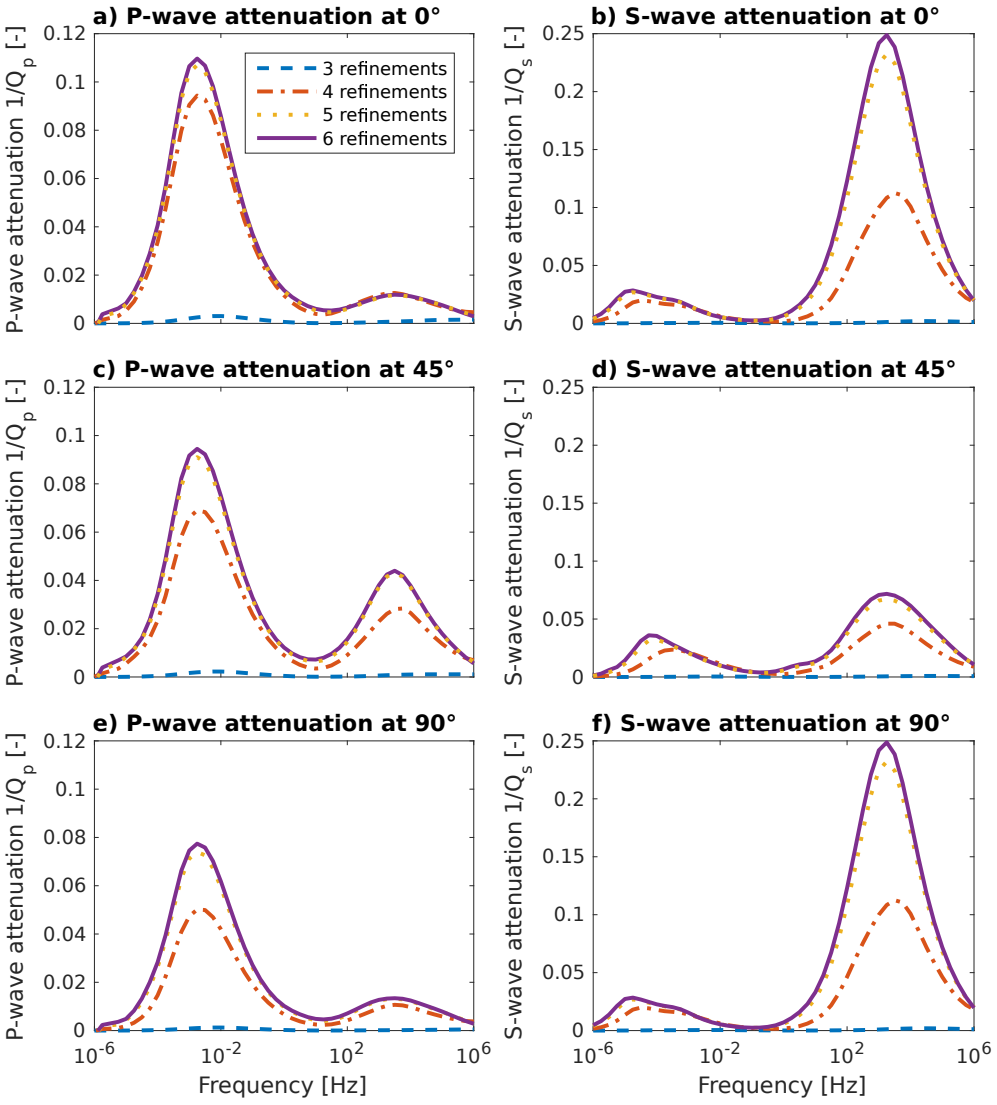

Figure 11: Seismic attenuation and velocity dispersion characteristics of the model shown in Figure 10 for four refinement levels. Three different incident angles θ are considered: (a,b) $\theta = 0°$, (c,d) $\theta = 45°$ and (e,f) $\theta = 90°$.